UVicSPACE: Research & Learning Repository

University of Victoria

Faculty of Science

Faculty Publications

Monte Carlo optimization of a GRID collimator for preclinical megavoltage ultra-high dose rate spatially-fractionated radiation therapy

Nathan Clements, Magdalena Bazalova-Carter, and Nolan Esplen

2022

© 2022 Clements et al. This is an open access article distributed under the terms of the Creative Commons Attribution License. https://creativecommons.org/licenses/by/4.0/

This article was originally published at:

https://doi.org/10.1088/1361-6560/ac8c1a

Citation for this paper:

Clements, N., Bazalova-Carter, M., & Esplen, N. (2022). Monte Carlo optimization of a GRID collimator for preclinical megavoltage ultra-high dose rate spatially-fractionated radiation therapy. Physics in Medicine & Biology, 67(18), 185001. https://doi.org/10.1088/1361-6560/ac8c1a

IOP Publishing Phys. Med. Biol. 67 (2022) 185001 https://doi.org/10.1088/1361-6560/ac8c1a

Physics in Medicine & Biology

IPEM Institute of Physics and Engineering in Medicine

OPEN ACCESS

RECEIVED
13 May 2022

REVISED
10 August 2022

ACCEPTED FOR PUBLICATION
23 August 2022

PUBLISHED
7 September 2022

Original content from this work may be used under the terms of the Creative Commons Attribution 4.0 licence.

Any further distribution of this work must maintain attribution to the author(s) and the title of the work, journal citation and DOI.

PAPER

Monte Carlo optimization of a GRID collimator for preclinical megavoltage ultra-high dose rate spatially-fractionated radiation therapy

Nathan Clements , Magdalena Bazalova-Carter and Nolan Esplen

Department of Physics and Astronomy, University of Victoria, Victoria, BC, Canada

E-mail: nathanclements2000@gmail.com

Keywords: GRID, spatially-fractionated radiation therapy, optimization, collimator, Monte Carlo, dosimetry

Abstract

Objective. A 2-dimensional pre-clinical SFRT (GRID) collimator was designed for use on the ultra-high dose rate (UHDR) 10 MV ARIEL beamline at TRIUMF. TOPAS Monte Carlo simulations were used to determine optimal collimator geometry with respect to various dosimetric quantities. *Approach*. The GRID-averaged peak-to-valley dose ratio (PVDR) and mean dose rate of the peaks were investigated with the intent of maximizing both values in a given design. The effects of collimator thickness, focus position, septal width, and hole width on these metrics were found by testing a range of values for each parameter on a cylindrical GRID collimator. For each tested collimator geometry, photon beams with energies of 10, 5, and 1 MV were transported through the collimator and dose rates were calculated at various depths in a water phantom located 1.0 cm from the collimator exit. *Main results*. In our optimization, hole width proved to be the only collimator parameter which increased both PVDR and peak dose rates. From the optimization results, it was determined that our optimized design would be one which achieves the maximum dose rate for a PVDR $\geqslant$5 at 10 MV. Ultimately, this was achieved using a collimator with a thickness of 75 mm, 0.8 mm septal and hole widths, and a focus position matched to the beam divergence. This optimized collimator maintained the PVDR of 5 in the phantom between water depths of 0–10 cm at 10 MV and had a mean peak dose rate of 3.06 $\pm$ 0.02 Gy s^{-1} at 0–1 cm depth. *Significance*. We have investigated the impact of various GRID-collimator design parameters on the dose rate and spatial fractionation of 10, 5, and 1 MV photon beams. The optimized collimator design for the 10 MV ultra-high dose rate photon beam could become a useful tool for radiobiology studies synergizing the effects of ultra-high dose rate (FLASH) delivery and spatial fractionation.

1. Introduction

In the context of modern radiation therapy (RT), widening the therapeutic window remains a critical priority for oncological research and continues to drive the development of new radiation modalities capable of minimizing normal tissue toxicity without compromising treatment efficacy. In recent years, novel techniques, including spatially-fractionated RT (SFRT) and FLASH RT, have emerged which are proving capable of realizing this objective.

FLASH RT is characterized by its use of ultra-high dose rates (UHDR; >40 Gy s^{-1}) and large-dose fractions delivered over very short time scales (often < 0.1 s) (Favaudon *et al* 2014, Wilson *et al* 2020). To date, numerous studies on FLASH have found that the sub-second, hypo-fractionated UHDR irradiations may permit a reduction in healthy-tissue toxicity following treatment- correspondingly termed the FLASH effect- while maintaining similar anti-tumor responses to conventional (low dose rate) radiotherapy (CRT) across various different animal models (mice, mini pigs, and cats) and types of tissue (brain, neural stem cells, and skin) (Favaudon *et al* 2014, Levy *et al* 2019, Vozenin *et al* 2019a, 2019). The irradiation time reduction in FLASH (<0.1

© 2022 The Author(s). Published on behalf of the Institute of Physics and Engineering in Medicine by IOP Publishing Ltd

s compared to 1–3 min in CRT) would allow for better patient throughput, reduced treatment planning complexities between fractions and the ability to 'freeze' target motion to theoretically improve target volume conformality. The biological mechanisms which underlie the FLASH effect and their physical and radiochemical underpinnings remain an active area of research. Transient cell hypoxia has been suggested as one leading hypothesis (Adrian *et al* 2020), but likely does not entirely account for the observed effects (Zhou *et al* 2020, Boscolo *et al* 2021). FLASH-RT has recently undergone its first human trial, with results published in 2019 stating the successful short-term outcomes relating to both tumor control and reduced toxicity (Bourhis *et al* 2019).

SFRT is the treatment of tumors using non-uniform dose distributions, which in megavoltage (MV) beams is often achieved using grid-patterned beam filters (GRID therapy) (Weisi *et al* 2020). Megavoltage GRID therapy has been shown to reduce near and late-term patient side-effects, cause objective cancer regression, and reduce toxicity to healthy tissue (Mohammed *et al* 1999). On top of these advantages over CRT, GRID therapy has proven effective while allowing for high precision, high biologically equivalent dose RT (Onishi *et al* 2007), and is conducive in the treatment of more radioresistant tumors (Gholami *et al* 2016). Compared to conventional hypo-fractionated techniques, such as stereotactic body RT or stereotactic ablative radiotherapy, GRID has not shown the same degree of normal-tissue toxicity when treating large tumors (Kang *et al* 2015). The bystander effect (Widel 2016), differential vascular damage, and anti-tumor immune responses are some of the primary radiobiological effects that have been suggested as contributing to the therapeutic advantage of GRID therapy (Weisi *et al* 2020). In the clinic, GRID therapy is primarily used on bulky tumors (Geoffrey *et al* 2012), especially head and neck tumors (Isabelle Choi *et al* 2019), generally as a neoadjuvant treatment ahead of a conventional RT regimen. In general, maximizing the peak-to-valley dose ratio (PVDR) has shown improvement in healthy tissue sparing (Dilmanian *et al* 2002).

Ultra-high dose rate irradiations are inherently well-suited to SFRT techniques, most notably with micrometric beam sizes, given the decrease in blurring or loss of the fractionated dose distribution that might otherwise occur due to respiratory or cardiosynchronous organ motion. In fact, synchrotron mini- and micro-beam therapies have long relied upon UHDR sources to mitigate this risk (Avraham Dilmanian *et al* 2006, Prezado *et al* 2011, Bartzsch *et al* 2020). Now, with the advent of FLASH RT, the question has been raised whether the FLASH effect might be a contributing variable to the surprising differential normal tissue responses that have been demonstrated using micro-SFRT techniques (Bartzsch *et al* 2020). Investigations on UHDR broad beam (i.e. FLASH) and spatially-fractionated fields delivered using a common source may be valuable to elucidate the degree to which SFRT-specific or FLASH effects might be contributing to the differential tissue responses which characterize these therapies. While a select few synchrotrons may facilitate UHDR micro-fractionation using low-energy x-rays (Montay-Gruel *et al* 2022, Smyth *et al* 2018), it remains valuable to study how macroscopic SFRT might be used synergistically with a variety of higher energy UHDR modalities, especially considering the range of particle types and beam energies which appear capable of eliciting the FLASH sparing effects (Bourhis *et al* 2019, Esplen *et al* 2020).

Currently, synchrotron sources offer a reliable source for kV UHDR x-ray fields which are readily suitable to SFRT techniques (Bartzsch *et al* 2020). However, the use of higher (i.e. MV) beam energies during FLASH are important for enabling treatment at greater depths in tissue and can alleviate the rapid depth-dose fall-off of kV x-rays. To this end, there remains a need to develop MV UHDR x-ray sources and an open question as to whether MV-compatible fractionated techniques, such as GRID therapy, might be adapted for use in higher energy FLASH-compatible beams.

In the present work, Monte Carlo (MC) simulations are leveraged to inform the design of an optimized mini-GRID collimator for use on a new FLASH-SFRT platform: an 8–10 MV UHDR x-ray source, which has been developed for the advanced rare isotope laboratory (ARIEL) beamline at TRIUMF (Vancouver, Canada) (Esplen *et al* 2022). A range of practical and hypothetical geometric collimator parameters and beam energies are simulated to identify the effects of each parameter at different energies. 10 MV photons were of particular interest due to a higher Bremsstrahlung production rate, which better facilitates UHDR irradiations when compared with lower-energy beams. Successful implementation of MV GRID treatments on this new irradiation platform (or those like it) will facilitate research into x-ray FLASH and SFRT therapies both independently and in combination using a common source with the aim of identifying potential synergistic effects that might promote improved therapeutic outcomes.

2. Materials and methods

In this study, Monte Carlo simulations were used to optimize a mini-GRID collimator with respect to the mean peak dose rate (NPDR) and the PVDR.

Table 1. Constant MC simulation parameters.

Parameter	Value
Collimator material	Tungsten
Slit material	Air
CSD	1.0 cm
Beam power	1 kW
Full width at half maximum	2.94 mm
Phantom material	Water
Phantom dimensions	$5 \times 5 \times 20$ cm^3
SCD	2.2 cm
Tungsten cylinder radius	2.0 cm[a]
World material	Air

[a] This was increased for the optimized collimator.

2.1. Simulation software

TOPAS v3.6 (Perl *et al* 2012, Faddegon *et al* 2020) was used to run all MC simulations. TOPAS is an extension of GEANT4 (Agostinelli *et al* 2003) that was created to simplify complex Monte Carlo simulations for medical physics (Perl *et al* 2012). The physics module used in this study was the "g4em-standard-opt4" package with a cutoff distance of 0.01 cm for all particles. All other physics parameters were left as the defaults. Topas's highly customizable geometries and layered mass geometries allowed for us to algorithmically change the collimator parameters using Python.

2.2. Source description

The input source used in this work was based on an MC beam model developed for the new UHDR (FLASH) x-ray irradiation platform designed for the ARIEL electron linear accelerator (e-linac) at TRIUMF (Esplen *et al* 2022). The ARIEL e-linac and FLASH irradiation platform have been built and commissioned to deliver up to 10 MeV electrons at currents of up to 0.1 mA (1 kW average power) in order to produce UHDR x-ray fields suitable for FLASH radiotherapy research. The photon beam has a full width at half maximum (FWHM) of 2.94 mm (see table 1). An x-ray beam collimation assembly has also been designed to accommodate an array of 3D-printed collimator inserts that conform to a predefined cylindrical form factor. The field sizes considered in this study are outside of the current maximum; however, it is expected that the current form factor will be adapted to accommodate the field sizes similar to those considered here.

For each of the GRID collimator configurations, we simulated a previously defined IAEA phase space input source (Esplen *et al* 2022), a 2.2 cm source-to-collimator distance (SCD, the distance from the phase space source to the collimator entrance) was assumed, and 10^6 original histories (initial electrons delivered to the target) were transported for the 10 and 5 MV beams. 10^6 electrons corresponded to $\sim 4.9e8$ photons for 10 MV and $\sim 2.1e8$ photons for 5 MV. In the case of the 1 MV beam, 10^7 original histories were simulated to alleviate the lower statistics of the lower energy beam, this corresponded to $\sim 1.6e8$ photons. All scored particles were used. To obtain reasonable statistics for the parameter study, we ran the full phase space 10 times for 10 and 5 MV, and 50 times for 1 MV, and averaged the results to obtain the mean dose rates for each energy. For the optimized collimator (see section 3.3), we instead ran the full phase space 20 times for the 10 and 5 MV beams, and 100 times for the 1 MV beam. The dose distribution results of all runs were then averaged for each energy, identical to the parameter study.

2.3. Component definitions and parameterizations

The simulated cylindrical tungsten collimator had a radius of 2.0 cm, while its thickness was varied between 40 and 90 mm. However, the radius was increased to 2.6 cm to fit the larger hole sizes and spacing of the optimized collimator. The tungsten comprising the collimator was defined in TOPAS with a density of 19.3 g cm^{-3} and atomic number 74. The air surrounding the geometry was predefined by TOPAS with mass density of 1.2 mg cm^{-3}. Finally, the rectangular 5 cm $\times$ 5 cm $\times$ 20 cm phantom used in this study was composed of water that was predefined by TOPAS with a density of 1.0 g cm^{-3}.

The parameters held constant for each simulation are listed in table 1. We varied the focus position (the distance from the beam spot to the entrance surface of the collimator), the thickness of the collimator (dimension along the beam axis), the source-side septal width, and the source-side hole width (see figure 1) to optimize the PVDR and the mean PDR. The default collimator parameter values (bold values in table 2) were used when the parameter in question was not the one being varied. The default collimator had a 50 mm thickness, a 22 mm focus position in order to match beam divergence, a 0.3 mm septal width (based on 3D-

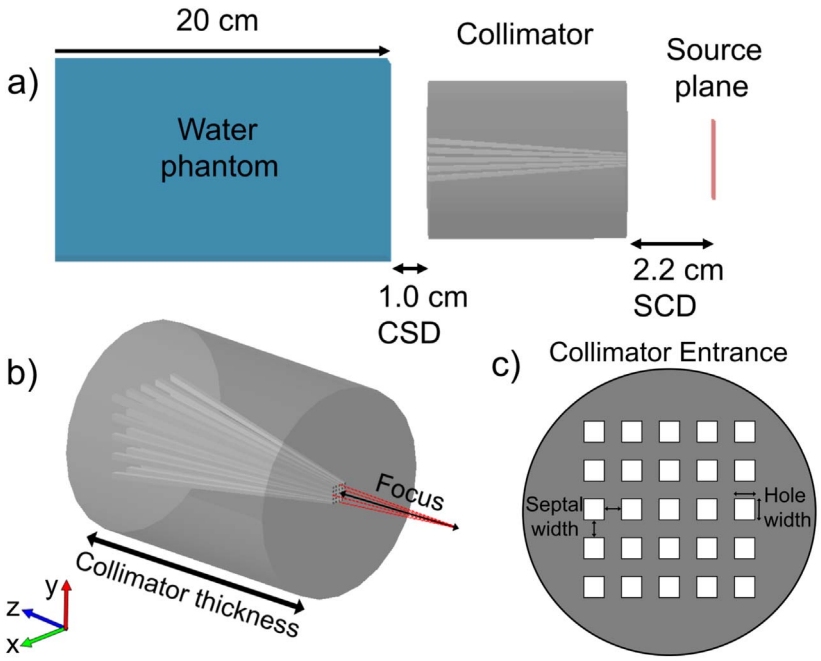

Figure 1. (a) Diagram of simulated apparatus indicating plane of x-ray source, beam collimator, phantom composed of water, source-to-collimator distance (SCD), and collimator-to-surface distance (CSD). (b) Diagram of collimator with collimator thickness and focus position parameters indicated. (c) Diagram of collimator entrance indicating septal width and hole width parameters.

Table 2. Parameters to be optimized.

Optimization parameters	Values (mm)
Focus position	12, **22**, 32, 42
Collimator thickness	40, **50**, 60, 70, 80, 90
Septal width	**0.3**, 0.4, 0.5, 0.6, 0.7, 0.8
Hole width	0.332, **0.432**, 0.532, 0.632, 0.732, 0.832

Bold indicates 'default' parameters.

printing limitations), and a 0.432 mm hole width. It should be noted that the exit-side holes and septal widths were determined from the entry-side hole and septal widths and the focus position.

2.4. Scoring

The summed dose to medium was recorded in a 5 cm × 5 cm × 20 cm water phantom comprising 12,500 (0.2 cm × 0.2 cm × 1 cm) voxels located at a collimator-to-surface distance (CSD) of 1.0 cm (the distance between the collimator exit and the surface of the water phantom). Phantom dose rates $\dot{D}$ were calculated from the simulated data using the following equation:

$$\dot{D} = \frac{D \cdot I}{N_H \cdot e}, \tag{1}$$

where D is the summed dose-to-medium value from the Monte Carlo simulations in gray, I is the beam current in amps, N_H is the number of original histories in the phase space (initial electrons), and e is the fundamental charge in coulombs.

2.5. Mean peak dose rate determination

1D and 2D profiles for all of the phantom dose results were produced (see figure 2) for each collimator configuration. We used the depth-averaged 2D profiles in 1 cm steps in calculating the mean PDR. Only the 2D profiles calculated at the 0–1 cm depth were considered in our parameter study. To determine the x and y coordinates of the peaks, we averaged each voxel row across the field width (x) and then found the five peak-containing rows using the 'find_peaks' function from scipy.signal (Virtanen *et al* 2020) and took them to be the y values for all peaks in that row. The x values were found identically only using the columns instead of rows. For

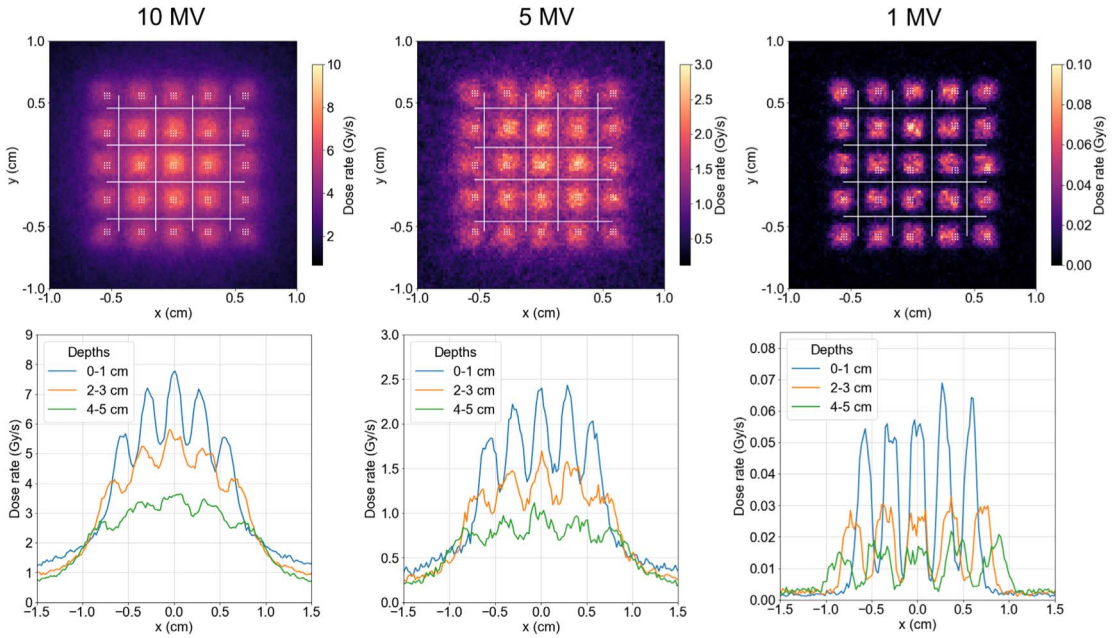

Figure 2. 2D and 1D dose rate profiles (averaged from 8 y-values around and including $y = 0$) in the water phantom from a 10, 5, and 1 MV photon beam passed through the default collimator. Data is shown for a depth of 0–1 cm for the 2D profiles and for three depths in the range of 0–5 cm for the 1D profiles. The voxels used in calculating the mean peak dose rate (PDR) and mean valley dose rate (VDR) are presented as white squares and lines, respectively.

better statistics, the eight voxels surrounding each peak voxel were included in the region of interest such that a mean of the 25 PDRs could be calculated (25 peaks × 9 voxels = 225 voxels). The uncertainty of the mean PDR was taken as $\Delta\langle \dot{D}_{\text{peak}} \rangle = \frac{1}{25}\sum_{n=1}^{25} \sigma_n^2$, where σ_n is the standard deviation of a peak containing nine voxels.

2.6. Calculating the peak-to-valley dose rate ratio

The PVDR was calculated using the mean PDR (as calculated above) divided by the mean VDR. The VDRs were found similarly to the PDRs by applying $f(x, y) = -f(x, y)$ (i.e. valleys become local maxima) within the range of the previously identified peak voxels. The mean VDR was then taken as the mean of the voxel rows and columns which defined the valleys. The uncertainty of the mean VDR was taken as $\Delta\langle \dot{D}_{\text{valley}} \rangle = \frac{1}{8}\sum_{n=1}^{8} \sigma_n^2$, where σ_n is the standard deviation of a row or column defining a valley.

With the mean VDR determined, the PVDR could be calculated as the mean PDR divided by the mean VDR. The uncertainty of the PVDR was calculated as

$$\Delta\text{PVDR} = \text{PVDR} \times \sqrt{\left(\frac{\Delta\langle \dot{D}_{\text{peak}} \rangle}{\text{PDR}}\right)^2 + \left(\frac{\Delta\langle \dot{D}_{\text{valley}} \rangle}{\text{VDR}}\right)^2}.$$

2.7. Examining the effects of depth on dose rate and PVDR

Mean PDR and PVDR were evaluated as functions of depth between 0 and 10 cm for the default collimator. PDR and PVDR were calculated as detailed in the previous sections.

To maximize the PVDR, and thus normal tissue sparing (Dilmanian *et al* 2002), our objective for the optimized collimator was a PVDR of 5 at 0–1 cm depth at 10 MV. This value was based on the results of our parameter study and the work of Martinez-Rovira *et al* who achieved a central PVDR of 12 at the surface, 5 at 5 cm depth and 3 at 10 cm depth for a 6 MV flattening filter-free photon beam in a Monte Carlo study.

After determining the PVDR and mean PDR results for all collimator configurations, we identified potential parameter combinations which could yield a PVDR of 5 for the 10 MV beam at 0–1 cm depth. To predict the parameter combinations that could produce a PVDR of 5, we approximated that the relative change in PVDR of each individual parameter from its default value would carry over the same relative effect. Simulations were run for a number of these parameter combinations until a PVDR >5 was found.

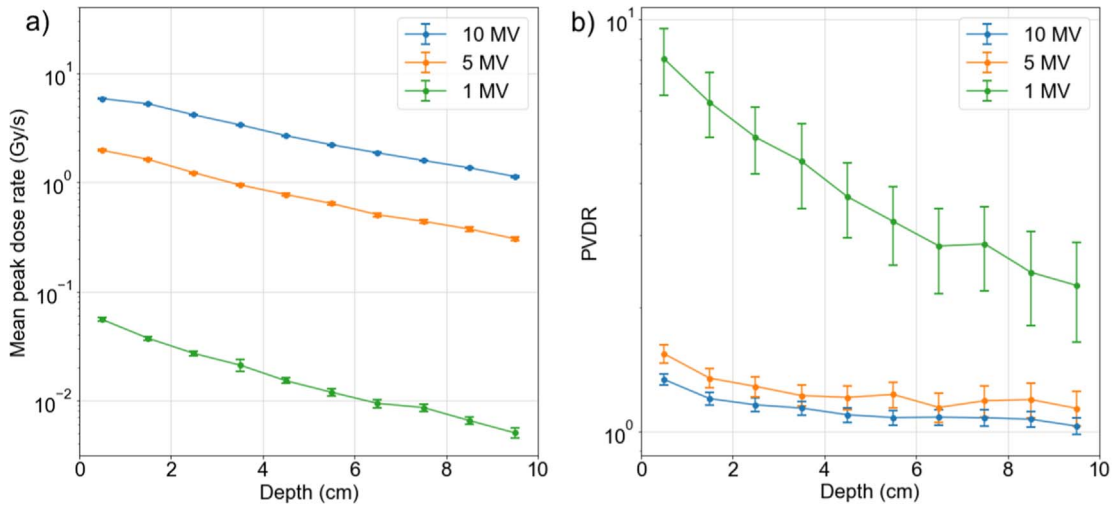

Figure 3. Mean peak dose rate (Gy/s) versus depth (cm) and PVDR versus depth for 10, 5, and 1 MV for default collimator parameters.

3. Results

3.1. Mean PDR and PVDR as functions of depth (default collimator)

The mean PDRs for 10, 5, and 1 MV are shown in figure 3. The mean PDR for all energies showed a decrease with increasing depth (see figure 3). From 0.5 to 9.5 cm, the mean PDR decreased by a factor of, in order of magnitude, 69 at 1 MV, followed by 6.50 at 5 MV, and 5.0 at 10 MV. The uncertainty also tended to increase with depth, consistent with a reduced signal-to-noise. The PVDR and mean PDR had inverse trends with energy, with the highest PVDRs occuring for 1 MV and the highest dose rates for 10 MV.

3.2. Optimization results

According to figure 4, for all energies, an inverse relationship is found between the PVDR and mean PDR for the collimator thickness, focus position, and septal width parameter variations. However, while increasing the hole width, both the mean PDR and the PVDR increased for 10 and 5 MV. For the 1 MV beam exclusively, hole-width variations did not change the PVDR across the range of widths used, within the bounds of the associated uncertainty. Additionally, the uncertainty on the mean PDRs remains low ($<$1.0%) down to depths of 10 cm across all beam energies.

Considering the collimator thickness variation results, decreases in mean PDR were observed for all three beam energies; however, we noticed that for the 10 and 5 MV data, the PVDR appeared to monotonically increase, whereas, for 1 MV the slope decreased monotonically with a presumed PVDR saturation of around 50 (see figure 4(a)). In this plot, increased uncertainty in the PVDR is observed as the collimator thickness was increased, most notably in the 1 MV case.

In varying the focus position, the mean PDR and PVDR monotonically increased and decreased for all energies, respectively, with increasing focus position (see figure 4(b)). Another element of note was the decrease in uncertainty on PVDR as the focus position increased.

The septal width optimization presented similar results to the collimator thickness optimization only with reduced rates of change (see figure 4(c)). For example, decreases in the mean PDR may be seen at all energies as the septal width increased, whereas the PVDR increased. The PVDR for the 1 MV beam appeared to plateau in a manner similar to the collimator thickness optimization.

Unlike the previous parameter studies, the hole width optimization displayed a monotonically-increasing relationship for the mean PDR and PVDR across the full range of widths, at least for the 5 and 10 MV beams. For the 1 MV beam, the PVDR did not change significantly considering the bounds of the associated uncertainty across the range of hole widths that we considered (see figure 4(d)). Therefore, we assumed a near constant PVDR at 1 MV for varying hole width, when all other parameters are kept constant. The PVDR and mean PDR for 5 and 10 MV, on the other hand, showed a clear positive slope.

3.3. Optimized collimator for a PVDR of 5 at 10 MV

Based on the results of figure 4, parameter combinations were determined that maximized the mean PDR while maintaining a PVDR of at least 5 for the 10 MV beam. Collimator parameter combinations which yielded such results were simulated. The final optimized collimator had a thickness of 75 mm, a focus position of 22 mm

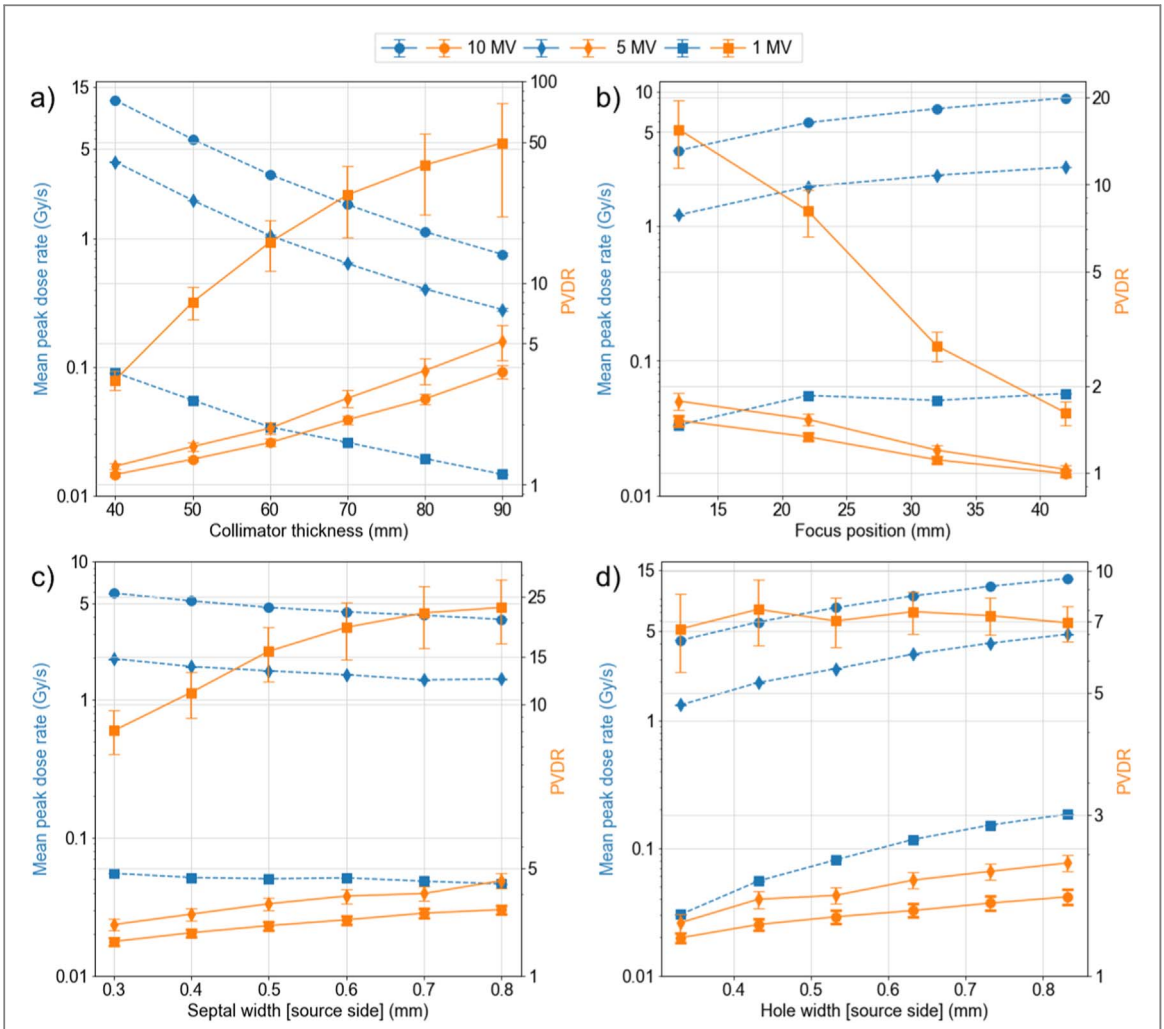

Figure 4. PVDR and mean peak dose rates (Gy/s) at 0–1 cm depth as functions of collimator thickness (a), focus position (b), septal width (c), and hole width (d). PVDR is represented as orange, solid curves, and the mean peak dose rate is given by the blue, dotted curves.

(matching the beam divergence), a source-side septal width of 0.8 mm, and a source-side hole width of 0.8 mm. It should also be noted that the radius of the collimator was increased from 20 to 26 mm to accommodate the consequent increase in field size.

The 2D dose rate profiles at 0–1 cm in depth, 1D dose profiles in depths from 0 to 10 cm, mean PDR with depth, and PVDR with depth plots are shown in figure 5 for 10, 5, and 1 MV. Considering the 2D dose rate profiles, a clear improvement in the distinction between the peaks and the valleys was observed when compared with the data in figure 2 for the 10 and 5 MV beams. For all energies, the peak edges were better defined in the 2D profiles. The 1D profiles similarly revealed defined peaks and valleys, down to 10 cm depth in water for all energies, but with higher energy presenting less noise. The PDR curves followed decays with the dose rate at 9.5 cm depth being ~4–5 × lower than that seen at 0.5 cm for 10 and 5 MV, however, ~12 × lower for 1 MV. Finally, the PVDR as a function of depth plot demonstrated no significant drop from 0 to 10 cm for 5 MV or 10 MV. In particular, the 10 MV plot showed no noticeable changes in PVDR across all depths, from 0 to 10 cm; while the 5 MV plot also did not show large changes with depth, the uncertainties in the data were larger and thus could obscure a real trend of decreasing PVDR with depth. Unlike the near-constant PVDRs for 10 and 5 MV, the 1 MV results for PVDR with depth decreased approximately exponentially following the mean PDR. For the 10 MV beam, averaging from 0 to 10 cm, the mean PVDR was (5.3 ± 0.4) and the 0–1 cm mean PDR was (3.06 ± 0.02 Gy s^{-1}). For 5 MV, the depth-averaged PVDR was (8.1 ± 1.1) and the 0–1 cm mean PDR was (0.68 ± 0.01 Gy s^{-1}). For 1 MV, the depth-averaged PVDR was (21 ± 5) and the 0–1 cm mean PDR was (0.0078 ± 0.0002 Gy s^{-1}).

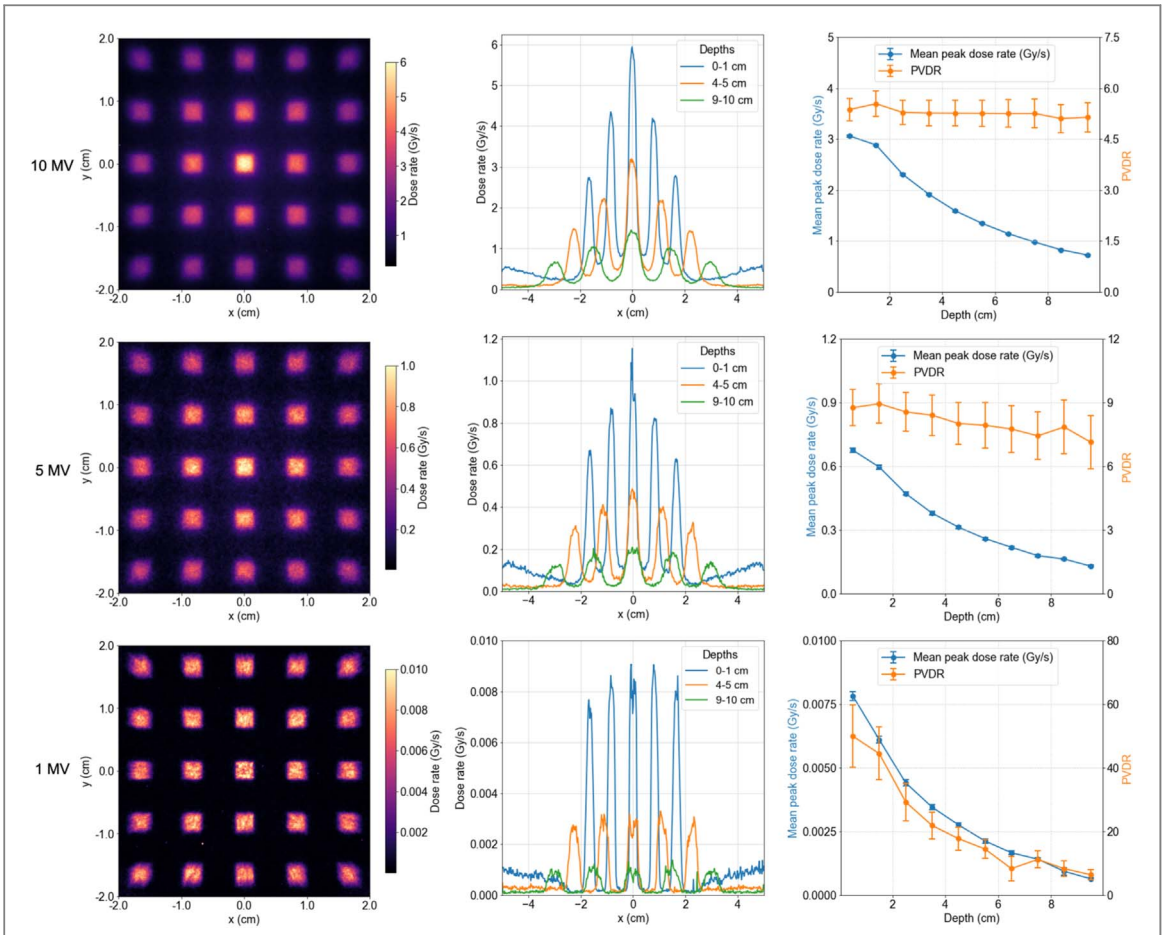

Figure 5. 2D dose rate profile in 0–1 cm, 1D dose rate profiles for depths from 0 to 10 cm, mean peak dose rate as a function of depth, and PVDR as a function of depth for 5 and 10 MV, optimized collimator.

4. Discussion

In this work, Monte Carlo simulations were conducted with the goal of optimizing a mini-GRID collimator for use on the 8–10 MV x-ray ARIEL beamline at TRIUMF (with our focus on 10 MV). A range of practical and hypothetical geometric collimator parameters were simulated at 1, 5, and 10 MV. We then examined the trends of PVDR and mean PDR as functions of these geometric parameters. Using these results, we selected an optimized parameter combination such that a PVDR of 5 could be maintained at 10 MV, with the results shown in figure 5.

As expected, the mean PDR in figure 3(a) decreased as depth increased for all energies due to x-ray attenuation. The dose fall off from 0.5 cm to 9.5 cm was 10x faster for 1 MV than for 5 and 10 MV due to the lower beam energy as well as the shorter range of 1 MV secondary electrons. The PVDR also decreased with depth in figure 3(b), suggesting that the PDRs were decreasing more rapidly than the VDRs.

The collimator thickness optimization shown in figure 4 presented a decrease in mean PDR as collimator thickness increased, likely due to the increased source-to-surface distance, from maintaining an SCD of 2.2 cm and CSD of 1 cm for all collimators, and possibly photon scatter. Conversely, the PVDR results for variable collimator thicknesses showed that the PVDR increased with collimator thickness. This trend is likely to be a result of the increased peak separation, which reduced the beamlet overlap that arises predominantly from the large secondary electron ranges and primary beam geometric penumbra. Thus, we also observe more well-defined valleys boasting lower dose rates. Peak separation was a function of the divergence of the focused hole geometries governed by the SCD and collimator thickness. Another element of interest in figure 4 was that the PVDR curves for 10 and 5 MV appeared to follow a different trend than for 1 MV. We suggest that this difference could be a result of the fact that 1 MV beam photons travelling through the divergent septa are attenuated to such a degree that any further increase predominantly affects changes to the, comparatively minor, collimator scatter contribution to the mean VDR due to increased peak separation.

In studying changes to the collimator focus position, we observed that the mean PDR for all energies was found to increase with the focus position while the PVDR decreased. It is interesting to note that the 1 MV PVDR

decreased much more rapidly, similar to the cases where the collimator thickness and septal width were varied. Since a shorter focus position corresponds to a larger exit-side septal width for the collimator, the PVDR increased with decreasing focus position. Our primary interest in examining the effects of the collimator focus position was to see if matching the beam divergence might yield higher dose rates at minimal expense to the PVDR. The results demonstrated that this was, somewhat surprisingly, not the case; in fact, the results demonstrate that it is not sufficient to simply back project to a point source when attempting to ensure optimal dose rate. This observation might be best understood given the fact that we have an extended source ((FWHM) = 2.94 mm) and a short SCD (2.2 cm).

The septal width optimization presented results that were similar to the collimator thickness optimization described previously. We saw a monotonic increase in PVDR, with the 1 MV trend line seeming to plateau at the largest septal width considered. Moreover, the mean PDR decreased as septal width increased, although not as quickly as it did for the case of increasing collimator thickness. The decrease in the mean PDR may be a result of the path length travelled by the photons being greater for the holes away from the center than that of the photons travelling through the center hole. The PVDR increase is likely a consequence of the lower VDRs, due to increased peak separation resulting from the increase in septal width. The hypothesized plateau in the PVDR at 1 MV may be a result of primary photons having to travel through the thicker septa, and thus being increasingly attenuated such that any further increase predominantly affects changes to the, comparatively minor, collimator scatter contribution to VDRs due to increased peak separation.

Considering the hole width optimization, an increase in the mean PDR and PVDR was observed for both 10 and 5 MV beams. For 1 MV, however, while an increase in the mean PDR with increased hole width was observed, the PVDR remained constant within the bounds of the uncertainty. The increase in the mean PDR for all beams was simply a result of the increased photon fluence reaching the phantom surface due to the larger holes (effective field size). The PVDR increase for the 10 and 5 MV beams meant that with increasing the hole width, the increase in the PDRs was greater than the associated increase of the VDRs. This trend was not so surprising because the septal width was kept constant and so substantial changes in the VDRs were not expected to occur. However, the increase in PVDR was not present in 1 MV simulations. Upon investigating the dose distributions, this effect could likely be attributed to a different angular distribution of the 1 MV beam compared to the 10 and 5 MV beams.

Finally, considering our optimized collimator and the results from figure 5, the 1D and 2D profiles for all energies showcased evident peaks and valleys. However, we noted that for decreased energy there was an increase in profile noise due to increased dose uncertainty. Interestingly, the dose rate increased towards the edges of the phantom in the 1D profiles for all energies in the 0–1 cm depth range. We propose that this may be due to the lack of backscatter for large oblique beam angles towards the phantom edge, caused by the highly divergent holes. The mean PDR for 10 and 5 MV presented near-identically shaped decreases with depth. For 1 MV, the mean PDR decreased faster similar to figure 3. The 10 MV PVDR plot as a function of depth was approximately constant within the range of the dose uncertainty; this was a favorable feature given that a high PVDR can be difficult to maintain in MV beams at greater depths. For 5 MV, the PVDR also proved to exhibit only slight decay with depth, though the trend was not statistically significant due to relatively large associated uncertainties. For 1 MV, the PVDR dropped off exponentially with the mean PDR, suggesting that the mean VDR was approximately constant for 1 MV, unlike for the 5 and 10 MV beams. The dose leakage into the valleys is known to be higher for the higher energies and is visible in the 1D profiles of figures 2 and 5. It is also similar to the PVDR trends seen in kV x-ray sources (Livingstone *et al* 2018).

There are few previous GRID therapy studies similar to this one in terms of the small beam size and the collimator dimensions, which used similar MV beam energies and thus allow for a comparison of the results presented here. One comparable Monte Carlo study on GRID therapy was conducted in 2017 testing the effects of a flattening filter-free Linac (Martínez-Rovira *et al* 2017). They simulated a cerrobend collimator with a similar grid pattern, only their smallest hole width was 3.0 mm with a septal width of 3.0 mm for a 6 MV beam (Martínez-Rovira *et al* 2017). In comparing the results for PVDR for this configuration and our own, we note that Martinez-Rovira *et al* achieved a central PVDR of 12 at the entrance, 6 at 2 cm depth, 5 at 5 cm depth and 3 at 10 cm depth. In the case of our optimized collimator at 5 MV, our PVDR was 8.88 ± 0.9 initially and 7.1 ± 1.2 at 9.5 cm. Keeping in mind that our collimator had a much smaller hole width and septal width, and that our PVDR was calculated using peaks and valleys from the entire GRID field rather than using the central peak, our results appear promising and motivate future investigations.

In a follow-up to this study, the tungsten mini-GRID collimator will be 3D printed in order to experimentally validate the results of this MC study.

5. Conclusion

In this study, we examined the effects of geometric parameters of a collimator for GRID therapy using Monte Carlo simulations. Feasible ranges of collimator parameters, specifically, collimator thickness, focus position, septal width, and hole width were tested to determine each parameter's impact on GRID-averaged PDR and PVDR between 0 and 10 cm depth in water. 1, 5, and 10 MV photon beam energies were used based on the source model for the new ARIEL UHDR (FLASH) x-ray platform at TRIUMF. From these results, an optimal set of collimator parameters was identified so as to achieve a PVDR of 5 with the 10 MV beam, while maximizing the mean PDR. The optimized collimator had a thickness of 75 mm, a focus position of 22 mm, a source-side septal width of 0.8 mm, and a source-side hole width of 0.8 mm. For the 10 MV beam, averaging from 0 to 10 cm, the mean PVDR was (5.3 ± 0.4) and the 0–1 cm mean PDR was (3.06 ± 0.02 Gy s^{-1}). The mean PDR for a PVDR of 5 was below the UHDR threshold of 40 Gy s^{-1}. In the future, we will examine 10 MV GRID therapy with peak dose rates above the UHDR threshold by modifying the target design.

Acknowledgments

The authors would like to thank the UVic Center for Advanced Materials and Related Technology (CAMTEC). This work was funded in part by an NSERC Discovery grant as well as the Canada Research Chairs program. This research was enabled in part by support provided by WestGrid (www.westgrid.ca) and Compute Canada (www.computecanada.ca).

ORCID iDs

Nathan Clements https://orcid.org/0000-0001-8911-997X
Nolan Esplen https://orcid.org/0000-0002-8347-8653

References

Adrian G, Konradsson E, Lempart M, Bäck S, Ceberg C and Petersson K 2020 The FLASH effect depends on oxygen concentration *Br. J. Radiol.* **93** 1106
Agostinelli S *et al* 2003 Geant4—a simulation toolkit *Nucl. Instrum. Methods Phys. Res. A* **506** 250–303
Avraham Dilmanian F, Zhong Z, Bacarian T, Benveniste H, Romanelli P, Wang R, Welwart J, Yuasa T, Rosen E M and Anschel D J 2006 Interlaced x-ray microplanar beams: a radiosurgery approach with clinical potential *Proc. Natl Acad. Sci.* **103** 9709–14
Bartzsch S, Corde S, Crosbie J C, Day L, Donzelli M, Krisch M, Lerch M, Pellicioli P, Smyth L M L and Tehei M 2020 Technical advances in x-ray microbeam radiation therapy *Fac. Eng. Inf. Sci. B* **65** 2
Boscolo D, Scifoni E, Durante M, Krämer M and Fuss M C 2021 May oxygen depletion explain the FLASH effect? A chemical track structure analysis *Radiother. Oncol.* **162** 68–75
Bourhis J *et al* 2019 Treatment of a first patient with FLASH-radiotherapy *Radiotherapy Oncol.* **139** 18–22
Dilmanian F A *et al* 2002 Response of rat intracranial 9L gliosarcoma to microbeam radiation therapy *Neuro-Oncol.* **4** 26–38
Esplen N, Mendonca M S and Bazalova-Carter M 2020 Physics and biology of ultrahigh dose-rate (FLASH) radiotherapy: a topical review *Phys. Med. Biol.* **65** 23
Esplen N M, Egoriti L, Paley W, Planche T, Hoehr C, Gottberg A and Bazalova-Carter M 2022 Design optimization of an electron-to-photon conversion target for ultra-high dose rate x-ray (FLASH) experiments at TRIUMF *Phys. Med. Biol.* **67** 10
Faddegon B, Ramos-Méndez J, Schuemann J, McNamara A, Shin J, Perl J and Paganetti H 2020 The TOPAS tool for particle simulation, a Monte Carlo simulation tool for physics, biology and clinical research *Phys. Med.* **72** 114–21
Favaudon V *et al* 2014 Ultrahigh dose-rate FLASH irradiation increases the differential response between normal and tumor tissue in mice *Sci. Transl. Med.* **6** 245
Geoffrey N, Mohiuddin M M, Vander Walde N, Goloubeva O, Ha J, Yu C X and Regine W F 2012 High-dose spatially fractionated GRID radiation therapy (SFGRT): a comparison of treatment outcomes with Cerrobend versus MLC SFGRT *Int. J. Radiat. Oncol., Biol., Phys.* **82** 1642–9
Gholami S, Nedaie H A, Longo F, Ay M R, Wright S and Meigooni A S 2016 Is grid therapy useful for all tumors and every grid block design? *J. Appl. Clin. Med. Phys.* **17** 206–19
Isabelle Choi J, Daniels J, Cohen D, Li Y, Ha C S and Eng T Y 2019 Clinical outcomes of spatially fractionated GRID radiotherapy in the treatment of bulky tumors of the head and neck *Cureus* **11** 5
Kang K H, Okoye C C, Patel R B, Siva S, Biswas T, Ellis R J, Yao M, Machtay M and Lo S S 2015 Complications from stereotactic body radiotherapy for lung cancer *Cancers* **7** 981–1004
Levy K, Rafat M, Casey K and Rankin E 2019 Total abdominal ultra-rapid flash irradiation decreases gastrointestinal toxicity compared to conventional radiation *Gynecol. Oncol.* **154** 75
Livingstone J, Stevenson A W, Häusermann D and Adam J F 2018 Experimental optimisation of the x-ray energy in microbeam radiation therapy *Phys. Med.* **45** 156–61
Martínez-Rovira I, Puxeu-Vaqué J and Prezado Y 2017 Dose evaluation of grid therapy using a 6 MV flattening filter-free (FFF) photon beam: A Monte Carlo study *Med. Phys.* **44** 5378–83
Mohammed M, Fujita M, Regine W F, Megooni A S, Ibbott G S and Ahmed M M 1999 High-dose spatially-fractionated radiation (GRID): a new paradigm in the management of advanced cancers *Int. J. Radiat. Oncol., Biol., Phys.* **45** 721–7
Montay-Gruel P, Corde S, Laissue J A and Bazalova-Carter M 2022 FLASH radiotherapy with photon beams *Med. Phys.* **49** 2055–67

Onishi H et al 2007 Hypofractionated stereotactic radiotherapy (HypoFXSRT) for stage I non-small cell lung cancer: updated results of 257 patients in a japanese multi-institutional study *J. Thoracic Oncol.* **2** 94–100

Perl J, Shin J, Schümann J, Faddegon B and Paganetti H 2012 TOPAS: an innovative proton Monte Carlo platform for research and clinical applications *Med. Phys.* **39** 6818–37

Prezado Y, Sarun S, Gil S, Deman P, Bouchet A and Duc G L 2011 Increase of lifespan for glioma-bearing rats by using minibeam radiation therapy *Journal of Synchrotron Radiation* **19** 60–5

Smyth L M L, Donoghue J F, Ventura J A, Livingstone J, Bailey T, Day L R J, Crosbie J C and Rogers P A W 2018 Comparative toxicity of synchrotron and conventional radiation therapy based on total and partial body irradiation in a murine model *Sci. Rep.* **8** 1–11

Virtanen P et al 2020 SciPy 1.0: fundamental algorithms for scientific computing in python *Nat. Methods* **17** 261–72

Vozenin M-C, Fornel P D, Petersson K, Favaudon V, Jaccard M, Germond J-F, Petit B, Burki M, Ferrand G, Patin D et al 2019 The advantage of flash radiotherapy confirmed in mini-pig and cat-cancer patients the advantage of flash radiotherapy *Clin. Cancer Res.* **25** 35

Vozenin M C, Hendry J H and Limoli C L 2019a Biological benefits of ultra-high dose Rate FLASH radiotherapy: sleeping beauty awoken *Clin. Oncol.* **31** 407–15

Weisi Y et al 2020 Spatially fractionated radiation therapy: history, present and the future *Clin. Transl. Radiat. Oncol.* **20** 30

Widel M 2016 Radiation induced bystander effect: from *in vitro* studies to clinical application *Int. J. Med. Phys., Clin. Eng. Radiat. Oncol.* **5** 1–17

Wilson J D, Hammond E M, Higgins G S and Petersson K 2020 Ultra-high dose rate (FLASH) radiotherapy: silver bullet or fool's gold? *Front. Oncol.* **9** 1563

Zhou S, Zheng D, Fan Q, Yan Y, Wang S, Lei Y, Besemer A, Zhou C and Enke C 2020 Minimum dose rate estimation for pulsed FLASH radiotherapy: a dimensional analysis *Med. Phys.* **47** 3243–9